RSC Advances

PAPER

View Article Online
View Journal | View Issue

Cite this: *RSC Adv.*, 2022, **12**, 16706

Structures, and electronic and spectral properties of single-atom transition metal-doped boron clusters MB_{24}^- (M = Sc, Ti, V, Cr, Mn, Fe, Co, and Ni)†

Shi-Xiong Li, *[a] Yue-Ju Yang,[a] De-Liang Chen[a] and Zheng-Wen Long[b]

A theoretical study of geometrical structures, electronic properties, and spectral properties of single-atom transition metal-doped boron clusters MB_{24}^- (M = Sc, Ti, V, Cr, Mn, Fe, Co, and Ni) is performed using the CALYPSO approach for the global minimum search, followed by density functional theory calculations. The global minima obtained for the MB_{24}^- (M = Sc, Ti, V, and Cr) clusters correspond to cage structures, and the MB_{24}^- (M = Mn, Fe, and Co) clusters have similar distorted four-ring tubes with six boron atoms each. Interestingly, the global minima obtained for the NiB_{24}^- cluster tend to a quasi-planar structure. Charge population analyses and valence electron density analyses reveal that almost one electron on the transition-metal atoms transfers to the boron atoms. The electron localization function (ELF) of MB_{24}^- (M = Sc, Ti, V, Cr, Mn, Fe, Co, and Ni) indicates that the local delocalization of MB_{24}^- (M = Sc, Ti, V, Cr, and Ni) is weaker than that of MB_{24}^- (M = Mn, Fe, and Co), and there is no obvious covalent bond between doped metal and B atoms. The spin density and spin population analyses reveal that open-shell MB_{24}^- (M = Ti, Cr, Fe, and Ni) has different spin characteristics which are expected to lead to interesting magnetic properties and potential applications in molecular devices. The polarizability of MB_{24}^- (M = Sc, Ti, V, Cr, Mn, Fe, Co, and Ni) shows that MB_{24}^- (M = Mn, Fe, and Co) has larger first hyperpolarizability, indicating that MB_{24}^- (M = Mn, Fe, and Co) has a strong nonlinear optical response. Hence, MB_{24}^- (M = Mn, Fe, and Co) might be considered as a promising nonlinear optical boron-based nanomaterial. The calculated spectra indicate that MB_{24}^- (M = Sc, Ti, V, Cr, Mn, Fe, Co, and Ni) has different and meaningful characteristic peaks that can be compared with future experimental values and provide a theoretical basis for the identification and confirmation of these single-atom transition metal-doped boron clusters. Our work enriches the database of geometrical structures of doped boron clusters and can provide an insight into new doped boron clusters.

Received 18th April 2022
Accepted 30th May 2022

DOI: 10.1039/d2ra02500k

rsc.li/rsc-advances

1. Introduction

Clusters are relatively stable microscopic or submicroscopic aggregates composed of several to thousands of atoms, molecules or ions, which have completely different structures and physical properties from bulk, and are also transition states from atoms to solid matter. Clusters are ideal models for correlating macroscopic properties and microscopic structures of substances, and cluster research is of great significance to deeply understand the laws of matter transformation. The physical properties of clusters are dependent on their size and shape, which can be changed to give them different physical properties owing to the quantum effect of electrons. Study of the structure and physical properties of clusters can provide guidance for the design and manufacture of new materials and new devices at the atomic level. The unique properties of clusters and doped clusters make their research a vibrant field of cluster science. For example, the emergence of fullerene C_{60} is a new breakthrough in nanomaterials and nanotechnology,[1] and the discovery of carbon nanotubes and graphene[2,3] promoted carbon nanomaterials to become a vibrant scientific field. The boron atom, with only three valence electrons (one less than carbon), can form polycentric chemical bonds and produce several interesting structures and properties.[4–9] Experimental studies have found that anionic pure boron clusters, B_n^-, with less than 38 atoms have a planar or quasi-planar structure.[10,11] Theoretical studies have found that neutral pure boron clusters of different sizes of B_n have planar, tubular, cage-like, or other three-dimensional structures.[4,8,12–14] Until 2014, scientists had been exploring whether boron could also form caged fullerene

[a]*School of Physics and Electronic Science, Guizhou Education University, Guiyang 550018, Guizhou, People's Republic of China. E-mail: leesxoptics@163.com*

[b]*College of Physics, Guizhou University, Guiyang 550025, Guizhou, People's Republic of China*

† Electronic supplementary information (ESI) available. See https://doi.org/10.1039/d2ra02500k

structures, but had been unable to experimentally determine the existence of caged boron clusters. In 2014, the cage-type all-boron cluster borospherene B_{40}^- was experimentally found.[15] Borospherene B_{40}^- exhibits a hollow cage-like structure, but has different electronic structures and properties from C fullerenes. B_{40}^- is the second inorganic non-metallic cage-like cluster that has been fully confirmed experimentally and theoretically after C_{60} and produced a lot of research on boron clusters.[16–24] In 2015, graphene's brother borophene was synthesized on the Ag(111) base,[25] and the basic unit of borophene happened to be a deformed B_7 cluster. In 2021, uniform and large-scale (millimeter-scale) bilayer borophene was synthesized on the surface of Cu(111).[26] Compared with borophene, bilayer borophene is more difficult to oxidize. Almost in the same period, a borophene crystal form comparable to graphene was experimentally synthesized,[27] and atomic hydrogen was used to hydrogenate borophene to synthesize borophene that can be stable in the external environment for a week. The discovery of borospherene and borophene provides important clues for the development of new boron materials. In view of the difference in electronic structure with fullerenes and carbon nanomaterials, boron clusters and low-dimensional boron nanostructures can offer new ideas and technologies for new nanomaterials and nano devices.

Similar to fullerenes, doped (especially for mono-atom) boron clusters can produce new structures or properties.[18,20–22,28–41] For example, B_{20}^-, B_{22}^-, and B_{24} have a quasi-planar, quasi-planar, and double-ring tubular structure,[10,42] respectively. However, after adding alkali metal atoms, both LiB_{20}^- and MB_{22}^- (M = Na, K) possess a double-ring tubular structure and Li_2B_{24} possesses a three-ring tubular structure.[29,43,44] In addition, Li-, Na-, or K-doped B_{40} is expected to become a nonlinear optical nanomaterial.[21] Because of their rich electronic structure characteristics, transition metal atom can combine with boron clusters to produce rich structures and properties. For example, the quasi-planar B_{12} cluster has a semi-sandwich structure after being doped with a metal atom such as Co and Rh.[6,28] Neutral B_{24} has a double-ring tubular structure, while TiB_{24} and CrB_{24} have a cage structure after doping with one Ti or Cr atom.[45] The single-atom Sc- or Ti-doped B_{40} is expected to become a hydrogen storage material,[18,20,22] doped boron clusters MB_{12}^- (M = Co, and Rh) can enhance chemical activity,[31] and the Co-doped B_{40} is expected to be applied in molecular devices.[30] Experimental and theoretical studies have found that transition metal atom doped boron clusters ReB_n^- (n = 3–4, 6, 8–9), MnB_n^- (n = 6, 16), BiB_n^- (n = 6–8), CoB_{16}^-, $La_2B_n^-$ (n = 10–11) and $La_3B_{18}^-$ have various unique structures.[33–41] Metal encapsulation is known as an effective approach to modify the chemical bonding and occupancy of energy levels of clusters. Metal (or metal cluster) encapsulation has also been suggested as a possible synthesis pathway for stabilizing the unstable boron fullerene analogue. Therefore, the study of transition metal-doped boron clusters provides important theoretical guidance for the study of new structures and new properties of boron clusters and the preparation of new boron nanomaterials. Herein, to obtain the structures and properties of transition metal-doped boron clusters MB_{24}^- (M = Sc, Ti, V, Cr, Mn, Fe, Co, and Ni), extensive research has been conducted on the geometric structure, spectral properties, and electronic structure using the CALYPSO approach,[46] in combination with the density functional theory method PBE0.[47] The calculation results will be useful for future experimental data of MB_{24}^- (M = Sc, Ti, V, Cr, Mn, Fe, Co, and Ni).

2. Computational methods

Geometric structure searches of MB_{24}^- (M = Sc, Ti, V, Cr, Mn, Fe, Co, and Ni) clusters were implemented using particle swarm optimization (CALYPSO) software. CALYPSO is a powerful cluster structure search method, which has been successfully applied to boron and doped boron clusters.[14,29] The PBE0/3-21G level was used for the preliminary structural search. In each generation, 70% of the structures were produced by particle swarm optimization (PSO) operations, while the others were randomly generated. There were nearly 2000 isomers initially obtained for each doped boron cluster. In addition, some plane structural constructions were also produced by the artificial bee colony algorithm (ABCluster) software[48] at the PBE0/3-21G level.

Low-energy structures were then fully optimized at the PBE0/6-311+G* and TPSSH/6-311+G* levels.[47,49,50] Moreover, density functional theory with dispersion correction (DFT-D3) was tested in the energy calculation.[51] At present, there are many methods of dispersion correction, such as dispersion-corrected atom-centered potentials (DCACPs), functional with van der Waals corrections (vdW-DF), dispersion correction as an add-on to standard Kohn–Sham density functional theory (DFT-D3) *etc.*[51] The DFT-D3 method is more advantageous,[52] and can be performed in Gaussian 16 software. We used the PBE0/6-311+G(d) and PBE0-D3/6-311+G(d) methods to calculate the low-energy structures of MB_{24}^- (M = Sc, Ti, V, Cr, Mn, Fe, Co, and Ni), and the results show that the relative energy trend of isomers (low-energy structures) in each cluster is found to be almost the same by using two methods. Moreover, PBE0/6-311+G(d) and PBE0-D3/6-311+G(d) methods were tested in the calculation of infrared spectra, Raman spectra, and polarizability of lowest energy structure for NiB_{24}^-, and the results also show that the infrared spectra, Raman spectra, and polarizability are found to be almost the same by using two methods. Therefore, density functional theory with dispersion correction (PBE0-D3) does not have a significant effect on the results, however, it further verifies the reliability of the PBE0 method. In addition, the PBE0/6-311+G* level is reliable method for boron cluster,[15,53–57] specifically, theoretical calculation results with the PBE0/6-311+G* level agrees with the experimental results.[15] Therefore, after the geometry optimizations, frequency analyses, electronic structures and spectroscopic properties were studied at the PBE0/6-311+G* level. All computations were performed using Gaussian 16 software.[58] The dipole moment, spin density, atomic charge, and electronic structures can be obtained directly from the calculation results of geometry optimizations. The harmonic frequency can be obtained from the calculation results of frequency analyses (add keyword Freq in Gaussian 16). All analyses and various types of isosurface map drawings were realized using the Multiwfn 3.7(dev) code.[59]

The energy of a system in the weak and uniform external electric field **F** can be revealed as[21,60]

$$E(\mathbf{F}) = E(0) - \boldsymbol{\mu}_0\mathbf{F} - \frac{1}{2}\boldsymbol{\alpha}\mathbf{F}^2 - \frac{1}{6}\boldsymbol{\beta}\mathbf{F}^3 - \ldots \quad (1)$$

where $E(0)$ is the molecular total energy without the external electric field, $\boldsymbol{\mu}_0$ is dipole moment, $\boldsymbol{\alpha}$ is polarizability, which is a matrix (second rank tensor), $\boldsymbol{\beta}$ is first hyperpolarizability, which is a third rank tensor and known as second order nonlinear optical response (NLO) coefficient. Isotropic average polarizability α can be defined as[60]

$$\alpha = (\alpha_{xx} + \alpha_{yy} + \alpha_{zz})/3 \quad (2)$$

Anisotropy of polarizability can be defined as[61]

$$\Delta\alpha = \sqrt{\left[(\alpha_{xx} - \alpha_{yy})^2 + (\alpha_{xx} - \alpha_{zz})^2 + (\alpha_{yy} - \alpha_{zz})^2 + 6(\alpha_{xy}{}^2 - \alpha_{xz}{}^2 + \alpha_{yz}{}^2)\right]/2} \quad (3)$$

Magnitude of first hyperpolarizability β_0 can be defined as[21]

$$\beta_0 = \sqrt{(\beta_x{}^2 + \beta_y{}^2 + \beta_z{}^2)} \quad (4)$$

where $\beta_x = \frac{3}{5}(\beta_{xxx} + \beta_{xyy} + \beta_{xzz})$, $\beta_y = \frac{3}{5}(\beta_{yyy} + \beta_{yxx} + \beta_{yzz})$, $\beta_z = \frac{3}{5}(\beta_{zzz} + \beta_{zxx} + \beta_{zyy})$. These components can be calculated using Gaussian 16 software and analyzed using Multiwfn 3.7(dev) code.

3. Results and discussion

3.1 Structures and electronic properties

The five low-energy structures of transition metal-doped boron clusters MB_{24}^- (M = Sc, Ti, V, Cr, Mn, Fe, Co, and Ni) are shown in Fig. S1–S8 (ESI†). As shown in Fig. S1–S8,† the relative energy trend of five low-energy structures in each cluster is found to be almost the same by using PBE0/6-311+G*, TPSSH/6-311+G*, and PBE0-D3/6-311+G* levels. The calculation results show that the low-energy structures of MB_{24}^- (M = Sc, Ti, V, Cr, Mn, Fe, and Co) tend to form cage structure or tubular structure, and NiB_{24}^- tend to form quasi-planar structure. Early research found that B_{24} has a double-ring tubular structure, and B_{24}^- has a planar structure. It can be seen from Fig. 1 and the calculated results that after adding metal atoms, the lowest energy structures MB_{24}^- (M = Sc, Ti, V, and Cr) have endohedral borospherene structures. The lowest energy structure TiB_{24}^- has high symmetry (D_{3h}), and the Ti atom is located at the center of the cage. The calculated results and Fig. 1 show that the lowest energy structures of VB_{24}^- and CrB_{24}^- have similar cage structures comprising 12 five-membered rings and there are four five-membered rings with a boron atom embedded in the center of five-membered rings. Among them, VB_{24}^- has higher symmetry (C_{2v}) than CrB_{24}^- (C_2), and the V atom is almost located at the center of the cage.

The calculated results and Fig. 2 show that the lowest energy structures of MB_{24}^- (M = Mn, Fe, and Co) have similar distorted four-ring tube with six boron atoms each. This structure can also be viewed as a distorted cage. In particular, the ring where the metal atom is located is not closed, further leading to an open seven-membered ring on the wall. MB_{24}^- (M = Mn, Fe, and Co) have low symmetry (C_s), and the doped atom is located at the center of a six-membered ring. Similar to tubular B clusters, these doped boron clusters are expected to become the basic unit of boron nanotube materials, which will be further synthesized into boron nanotubes. It can be seen from Fig. 2 that the lowest energy structure of NiB_{24}^- has quasi-planar structure similar to a warplane shape. The metal atom is located right at the nose, surrounded by an eight-membered boron ring. Similar to deformed B_7 cluster, the quasi-planar NiB_{24}^- is expected to become the basic unit of doped borophene, which will be further synthesized into borophene. In the following discussion, the main focus is on the study of the lowest energy structure.

Some of the ground-state parameters of transition metal-doped boron clusters MB_{24}^- (M = Sc, Ti, V, Cr, Mn, Fe, Co, and Ni) are listed in Table 1, including the lowest harmonic frequency, dipole moment, atomic charge on doped transition-metal atoms, and Mayer bond level.[62] The lowest harmonic frequency analysis (see Table 1 for the lowest harmonic frequencies of each cluster) confirmed that these lowest energy structures are indeed stable (no imaginary frequency). The charge population analysis shows that all the metal atoms show positive charges, indicating that electrons have been transferred to the boron atoms and the metal atoms have transferred almost one electron. Because there is more than one outer valence electron of doped atom, only a small part of the electrons has been transferred. Analysis shows that the Mayer bond level of the metal atom M and B atom of these clusters is between 0.05 and 0.55 and it is less than 1, indicating that no obvious covalent bond is formed between the metal atom and the B atom. Because TiB_{24}^- has high symmetry, D_{3h}, the dipole moment is 0. Among these nanoclusters MB_{24}^- (M = Sc, Ti, V, Cr, Mn, Fe, Co, and Ni), it is found that the closed-shell MB_{24}^- (M = Sc, V, Mn, and Co) clusters have large HOMO–LUMO gap of 3.49, 4.02, 2.22, and 3.14 eV, respectively. For the open-shell MB_{24}^- (M = Ti, Cr, Fe, and Ni) clusters, alpha HOMO–LUMO gaps are 3.84, 2.63, 3.17 and 1.91 eV, respectively, and beta HOMO–LUMO gaps are 1.97, 3.87, 2.45, and 2.03 eV, respectively. To show more clearly the influence of the transition metal-doping toward the electronic structure, total density of states (TDOS) of each cluster and partial density of states (PDOS) of the transition metal atom were analyzed using the Multiwfn 3.7(dev) code, as shown in Fig. S9 (ESI†). For the closed-shell MB_{24}^- (M = Sc, Mn, and Co), metal atoms contribute a part to HOMO and LUMO. However, for the closed-shell VB_{24}^-, V atom contributes nothing to HOMO and LUMO. For the open-shell TiB_{24}^-, alpha HOMO is entirely contributed

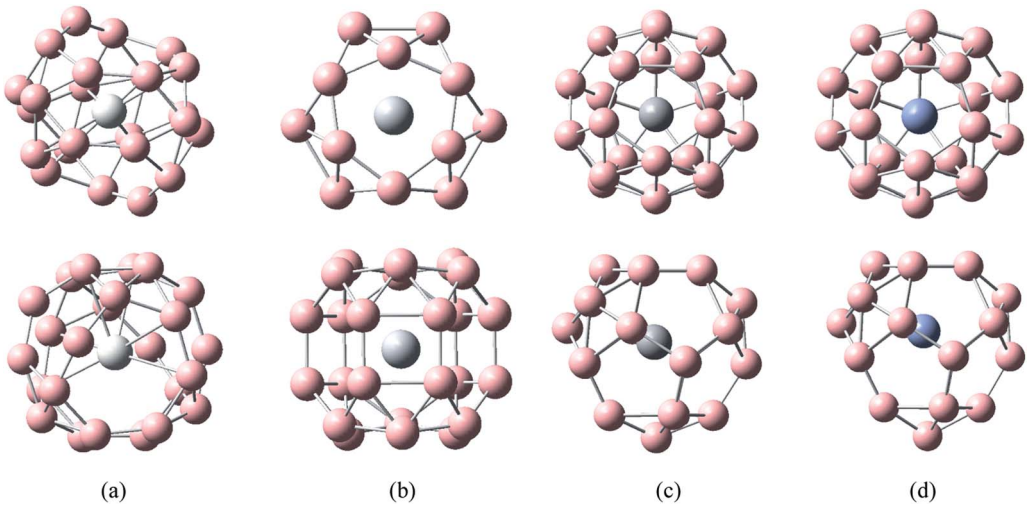

Fig. 1 Structures of doped boron clusters MB_{24}^- (M = Sc, Ti, V, and Cr). The upper row is top view and the bottom row is side view. (a) ScB_{24}^- C_2; (b) TiB_{24}^- D_{3h}; (c) VB_{24}^- C_{2v}; (d) CrB_{24}^- C_s.

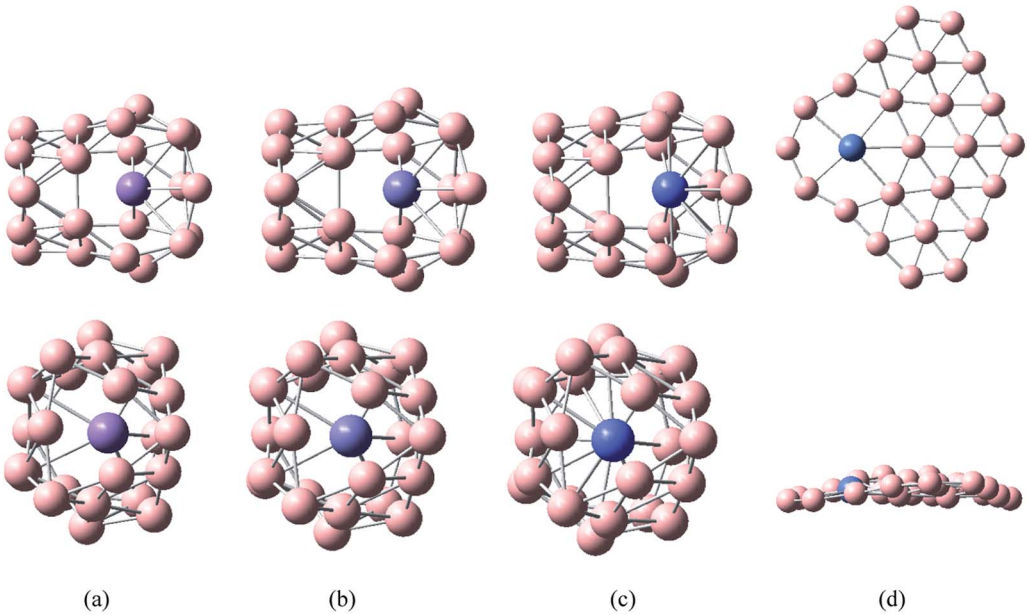

Fig. 2 Structures of doped boron clusters MB_{24}^- (M = Mn, Fe, Co, and Ni). The upper row is top view and the bottom row is side view. (a) MnB_{24}^- C_s; (b) FeB_{24}^- C_s; (c) CoB_{24}^- C_s; (d) NiB_{24}^- C_s.

by the orbitals of Ti atom, while Ti atom does not contribute to alpha LUMO, moreover, beta LUMO is mainly contributed by the orbitals of Ti atom, and Ti atom contributes a part to beta HOMO. For open-shell CrB_{24}^-, Cr atom contributes a part to alpha HOMO, alpha LUMO and beta LUMO, but Cr atom does not contribute to beta HOMO. For open-shell MB_{24}^- (M = Fe, and Ni), metal atoms contribute a part to alpha HOMO, alpha LUMO, beta HOMO, and beta LUMO. It can be seen from the Fig. S9(b, c, e, f, h, i, k and l)† that for open-shell MB_{24}^- (M = Ti, Cr, Fe, and Ni) clusters, the spin polarization of the electronic states of these systems is obvious.

Fig. S10–S12† show the electron localization function (ELF)[63] of the valence electrons of MB_{24}^- (M = Sc, Ti, V, Cr, Mn, Fe, Co, and Ni). ELF can well describe the delocalization (or localization) of electrons and chemical bonds. Under the same isosurface value, a wider connected area occupied by an isosurface map means that electron delocalization is easier, and a narrower connected area occupied by an isosurface map means that electron delocalization is relatively difficult. When the isosurface value is 0.60 (Fig. S10†), the isosurface maps of NiB_{24}^- are connected on the plane of the molecule and the isosurface maps of MB_{24}^- (M = Sc, Ti, V, Cr, Mn, Fe, and Co) are connected on the surface of the cage. Fig. S11† shows the ELF when the isosurface value is 0.70. With this isosurface value, the isosurface diagram of NiB_{24}^- is broken on the part of the molecule, and the isosurface diagrams of MB_{24}^- (M = Sc, Ti, V,

Table 1 Lowest frequencies, symmetry, charges on doped atom, dipole moments, and Mayer bond orders between doped metal atoms and B atoms, of MB_{24}^- (M = Sc, Ti, V, Cr, Mn, Fe, Co, and Ni). Charges on doped atom and Mayer bond orders are calculated at the PBE0/6-311G* level

	Lowest frequencies/cm^{-1}	Symmetry	Charges on doped atom	Dipole moments/debye	Mayer bond order between doped atom M and B atom
ScB_{24}^-	181	C_2	0.56	1.43	0.16–0.19
TiB_{24}^-	160	D_{3h}	0.69	0.00	0.16–0.20
VB_{24}^-	297	C_{2v}	0.70	2.22	0.21–0.26
CrB_{24}^-	234	C_s	0.81	2.45	0.16–0.26
MnB_{24}^-	212	C_s	0.85	1.07	0.06–0.55
FeB_{24}^-	212	C_s	0.89	2.65	0.05–0.47
CoB_{24}^-	198	C_s	0.90	3.21	0.10–0.38
NiB_{24}^-	40	C_s	0.92	0.14	0.28–0.39

Cr, Mn, Fe, and Co) are broken on the surface of the cage. Fig. S10–S11† also show that there is a wide blank area around the metal atom, showing that the metal atom does not form an obvious covalent bond with the surrounding B atoms, which is consistent with the Mayer bond level analysis. Fig. S12† shows the ELF when the isosurface value is 0.80. Under this isosurface value, all the isosurface maps of MB_{24}^- (M = Sc, Ti, V, Cr, and Ni) are disconnected and there are no connected regions. However, the isosurface maps of MB_{24}^- (M = Mn, Fe, and Co) show that there is still a connected area on the surface of the cage, indicating that the local delocalization of MB_{24}^- (M = Sc, Ti, V, Cr, and Ni) is weaker than the MB_{24}^- (M = Mn, Fe, and Co). Quasi-planar structure NiB_{24}^-, cage-type MB_{24}^- (M = Sc, Ti, V, and Cr) and tubular MB_{24}^- (M = Mn, Fe, and Co) are expected to become the basic units of boron nanomaterials and be further synthesized into borophene, boron nanotubes or other three-dimensional materials. Considering the electron delocalization characteristics of these clusters, they are expected to be applied to molecular devices or switches.

Fig. S13–S16† show the isosurface diagrams of valence electron density for MB_{24}^- (M = Sc, Ti, V, Cr, Mn, Fe, Co, and Ni) with isosurface values of 0.10, 0.14, 0.20 and 0.52, respectively. Electron density describes the characteristics of electron distribution. Under the same isosurface value, a fatter (represents the bigger volume and wider connected area occupied by an isosurface map) isosurface means more electrons and a thinner isosurface means fewer electrons. The isosurface diagram of Sc is the thinnest (disappeared) and that of Ni is the thickest under the same isosurface value of 0.10, indicating that the electron density of Sc is the minimum and the electron density of Ni is the highest. From the previous atomic charge population analysis, we found that the charges on Sc, Ti, V, Cr, Mn, Fe, Co, and Ni were 0.56, 0.69, 0.70, 0.81, 0.85, 0.89, 0.90 and 0.92, respectively. The valence electrons of Sc, Ti, V, Cr, Mn, Fe, Co, and Ni are 3, 4, 5, 6, 7, 8, 9, and 10, respectively, so when the transferred electrons are removed, the remaining valence electrons of Sc, Ti, V, Cr, Mn, Fe, Co, and Ni should be 2.44, 3.31, 4.3, 5.19, 6.15, 7.11, 8.10, and 9.08. From this, it can be inferred that under the same isosurface value, the isosurface map of the Ni atom is the thickest and that of Sc is the thinnest. In addition, because the B atom has three valence electrons in addition to part of the electrons transferred from the metal atom, it has between 3 and 4 valence electrons. Therefore, the electron density of the B atom should be greater than that of Sc but less than that of V, Cr, Mn, Fe, Co, and Ni atoms. The calculation results (isosurface diagrams of valence electron density) show that as the value of the isosurface increases, the isosurface diagram of the Sc atom will disappear first and that of the B atoms in the ScB_{24}^- will disappear later (as shown in Fig. S13(a) and S15(a)),† indicating that the electron density of the B atoms is greater than that of Sc. With the increase of the isosurface value, the isosurface diagrams of the B atoms in MB_{24}^- (M = V, Cr, Mn, Fe, Co, and Ni) will disappear first, and the electron density isosurfaces of M (V, Cr, Mn, Fe, Co, and Ni) atoms will disappear later (as shown in Fig. S15(c–h)†), indicating that the electron density of the B atoms is less than those of the M (M = V, Cr, Mn, Fe, Co, and Ni) atoms. The electron density isosurface diagrams are qualitatively consistent with the atomic charge analysis results.

Fig. 3 shows the isosurface diagram of the spin density of MB_{24}^- (M = Ti, Cr, Fe, and Ni) with open shell structure at the PBE0/6-311G* level. Spin density reveals the distribution of unpaired electrons (single electrons) in three-dimensional space. A positive spin density means that there are more alpha electrons than beta electrons, while a negative spin density means that there are more beta electrons than alpha electrons. Fig. 3 shows a spin density diagram for an isosurface value of 0.002. Green represents a positive value (alpha electrons), while blue represents a negative value (beta electrons). It can be seen from Fig. 3 that the unpaired single electrons of TiB_{24}^- are alpha electrons that are distributed on Ti and B atoms. The unpaired single electrons of CrB_{24}^-, FeB_{24}^-, and NiB_{24}^- are both alpha and beta electrons. For CrB_{24}^- system, part of the unpaired alpha electrons are distributed on the Cr atom and part of the unpaired alpha electrons are on one B atoms, and the unpaired beta electrons of CrB_{24}^- are distributed on the other B atoms. For FeB_{24}^- system, part of the unpaired alpha electrons are distributed on the Fe atom and part of the unpaired alpha electrons are on seven B atoms, and the unpaired beta electrons of FeB_{24}^- are distributed on the other B atoms. For NiB_{24}^- system, only a small part of the unpaired alpha electrons is on the Ni atom and most of the unpaired alpha electrons are on the B atoms, and the unpaired beta electrons of NiB_{24}^- are distributed on the two B atoms.

To further quantitatively analyze the distribution of unpaired single electrons on different atoms, the spin

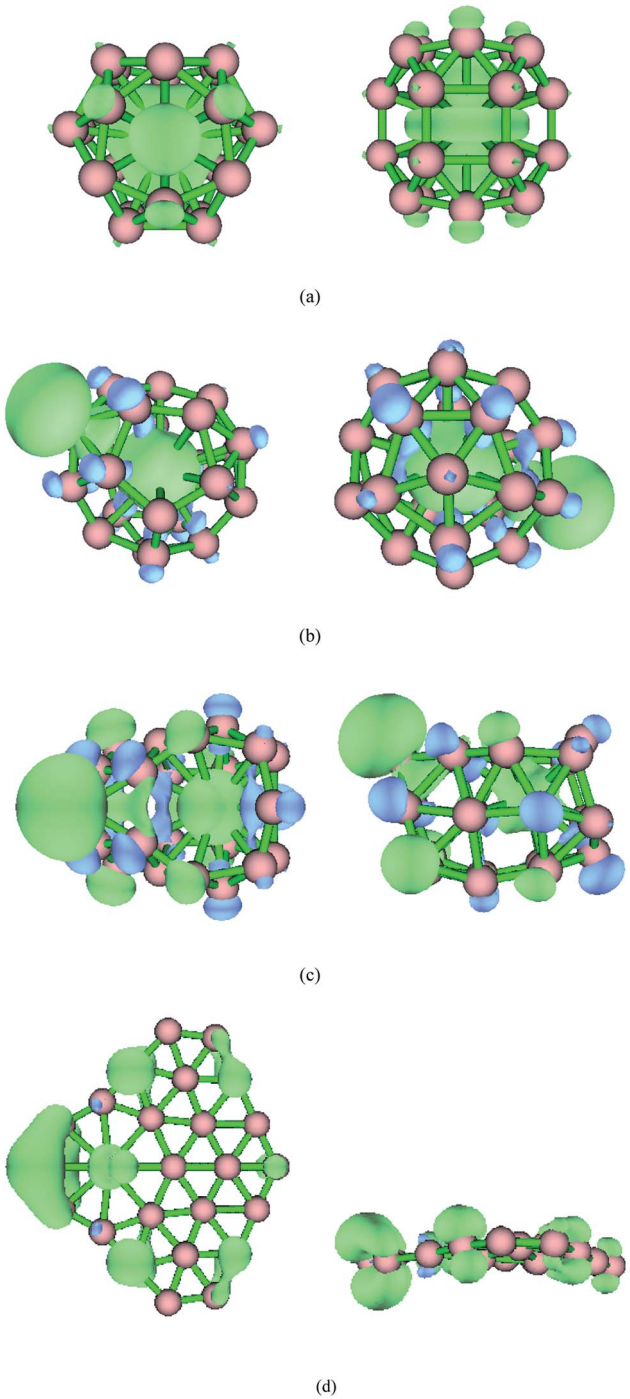

Fig. 3 Spin density with the isovalue set to 0.002. Green represents a positive value (alpha electrons), and blue represents a negative value (beta electrons). (a) TiB_{24}^-; (b) CrB_{24}^-; (c) FeB_{24}^-; (d) NiB_{24}^-.

population is calculated at the PBE0/6-311G* level. The spin population is defined as the alpha electron population minus the beta electron population. For example, if the spin population of an atom is one, the alpha electron population of this atom is one more than its beta electron population. A positive population corresponds to an alpha single electron, while a negative population corresponds to a beta single electron. The spin population analysis shows that there is one unpaired alpha electron in the TiB_{24}^- system, of which 0.54 is on the Ti atom and the remaining 0.46 is on the B atoms. This result is consistent with the spin density diagram (Fig. 3(a)). Although the total number of unpaired electrons in the CrB_{24}^-, FeB_{24}^-, and NiB_{24}^- systems are both 1, 1.64 unpaired alpha electrons and 0.64 unpaired beta electrons, 1.66 unpaired alpha electrons and 0.66 unpaired beta electrons, 1.24 unpaired alpha electrons and 0.24 unpaired beta electrons are distributed in the CrB_{24}^-, FeB_{24}^-, and NiB_{24}^- systems, respectively. For CrB_{24}^- system, 1.11 alpha electrons are on the Cr atom and 0.53 alpha electrons are on the one B atom, and the 0.64 beta electrons are distributed on the remaining B atoms. For FeB_{24}^- system, 0.75 alpha electrons are on the Fe atom and 0.91 alpha electrons are on the seven B atoms, and the 0.66 beta electrons are distributed on the remaining B atoms. For NiB_{24}^- system, 0.20 alpha electrons are on the Ni atom and 1.04 alpha electrons are on the ten B atoms, and the 0.24 beta electrons are distributed on the two B atoms. These results are also consistent with the spin density diagram of MB_{24}^- (M = Cr, Fe, and Ni). The spin density reflects chemical reactions or adsorption to a certain extent. The single electrons of TiB_{24}^- are all alpha electrons and distributed on the Sc and B atoms that can pair with free radicals or small molecules containing beta single electrons to form new covalent bonds. For the CrB_{24}^- system, one B atom with single alpha electrons can adsorb or react with free radicals or small molecules with single beta electron, while other B atoms with single beta electrons can adsorb or react with atoms, free radicals, or small molecules with alpha single electrons. Spin features of these clusters are expected to be applied to catalysis. In addition, these spin features are expected to produce interesting magnetic properties, which will further lead to potential applications in molecular devices.

3.2 Polarization properties

To understand the polarization properties of the clusters, the polarizability of the each cluster was calculated, including average isotropic polarizability α, anisotropic polarizability $\Delta\alpha$, and the first hyperpolarization β_0. α is also called the linear optical coefficient and $\Delta\alpha$ describes the response of the system to electric fields from different directions. The larger the value of $\Delta\alpha$, the stronger is the anisotropic response to the external electric field. The first hyperpolarizability is also called the second-order nonlinear optical (NLO) coefficient, which evaluates the nonlinear optical properties of molecules. It can be

Table 2 Polarizabilities of MB_{24}^- (M = Sc, Ti, V, Cr, Mn, Fe, Co, and Ni)

	α/a.u.	$\Delta\alpha$/a.u.	β_0/a.u.
ScB_{24}^-	342	11	2
TiB_{24}^-	320	9	0
VB_{24}^-	308	2	57
CrB_{24}^-	318	32	416
MnB_{24}^-	322	76	1673
FeB_{24}^-	324	75	1236
CoB_{24}^-	328	75	1100
NiB_{24}^-	457	416	494

seen from Table 2 that the isotropic polarizability of NiB_{24}^- is higher than that of MB_{24}^- (M = Sc, Ti, V, Cr, Mn, Fe, and Co), indicating that the bonding interactions between the atoms within NiB_{24}^- are stronger than those of MB_{24}^- (M = Sc, Ti, V, Cr, Mn, Fe, and Co), and NiB_{24}^- is more likely to be polarized by an external electric field. The anisotropic polarizability of VB_{24}^- is the smallest and that of NiB_{24}^- is the largest, indicating that VB_{24}^- has the weakest anisotropic response and NiB_{24}^- has the strongest response to an external electric field. It can be seen from Table 2 that the first hyperpolarizability of TiB_{24}^- is equal to 0, indicating that there is no nonlinear optical response. The first hyperpolarizability of ScB_{24}^- is 2, indicating that the nonlinear optical response is extremely small, and MB_{24}^- (M = Mn, Fe, and Co) have larger first hyperpolarizability, indicating that MB_{24}^- (M = Mn, Fe, and Co) have strong nonlinear optical response. Hence, the MB_{24}^- (M = Mn, Fe, and Co) might be considered as a promising nonlinear optical boron-based nanomaterial.

3.3 Photoelectron spectra

Photoelectron spectroscopy is powerful experimental technique to probe the electronic structure of cluster. Photoelectron spectroscopy in combination with theoretical calculations has been used to understand and identify the structures of size-selected boron clusters.[6,15,64] To facilitate future identifications of MB_{24}^- (M = Sc, Ti, V, Cr, Mn, Fe, Co, and Ni), the adiabatic detachment energies (ADEs) for MB_{24}^- (M = Sc, Ti, V, Cr, Mn, Fe, Co, and Ni) were calculated at the PBE0 level, then, we calculated the vertical detachment energies (VDEs) and simulated the photoelectron spectra for MB_{24}^- (M = Sc, Ti, V, Cr, Mn, Fe, Co, and Ni) with the time-dependent DFT (TD-DFT) method.[15,64,65] Adiabatic detachment energy of MB_{24}^- (M = Sc, Ti, V, Cr, Mn, Fe, Co, and Ni) represents the electron affinity (EA) of corresponding neutral MB_{24} (M = Sc, Ti, V, Cr, Mn, Fe, Co, and Ni). The larger EA can lead to the stronger probability of capturing an electron, *i.e.*, the neutral MB_{24} with larger EA is easier to capture an electron. MB_{24}^- (M = Sc, Ti, V, Cr, Mn, Fe, Co, and Ni) give the ground-state ADEs of 3.62 (ScB_{24}^-), 3.57 (TiB_{24}^-), 3.60 (VB_{24}^-), 1.92 (CrB_{24}^-), 3.08 (MnB_{24}^-), 3.11 (FeB_{24}^-), 3.01 (CoB_{24}^-) and 3.79 (NiB_{24}^-) eV, respectively. Among the MB_{24}^- (M = Sc, Ti, V, Cr, Mn, Fe, Co, and Ni), quasi-planar NiB_{24}^- has the largest ADE (3.79 eV), which is larger than the ADE (3.55 eV)[10] of quasi-planar B_{24}^-.

Fig. 4 presents the photoelectron spectra of MB_{24}^- (M = Sc, Ti, V, Cr, Mn, Fe, Co, and Ni). The predicted photoelectron spectra show that CrB_{24}^- has the lowest first vertical detachment energy (VDE) and the largest energy gap (about 1.51 eV) between the first and second bands. The first several bands of photoelectron spectra were used to identify boron clusters,[6,15] so we will focus on the bands at the low binding energy side. The first peaks of these photoelectron spectra(except for FeB_{24}^-) come from the calculated ground-state VDEs of ScB_{24}^-, TiB_{24}^-, VB_{24}^-, CrB_{24}^-, MnB_{24}^-, CoB_{24}^- and NiB_{24}^- at 3.78, 3.73, 3.86,

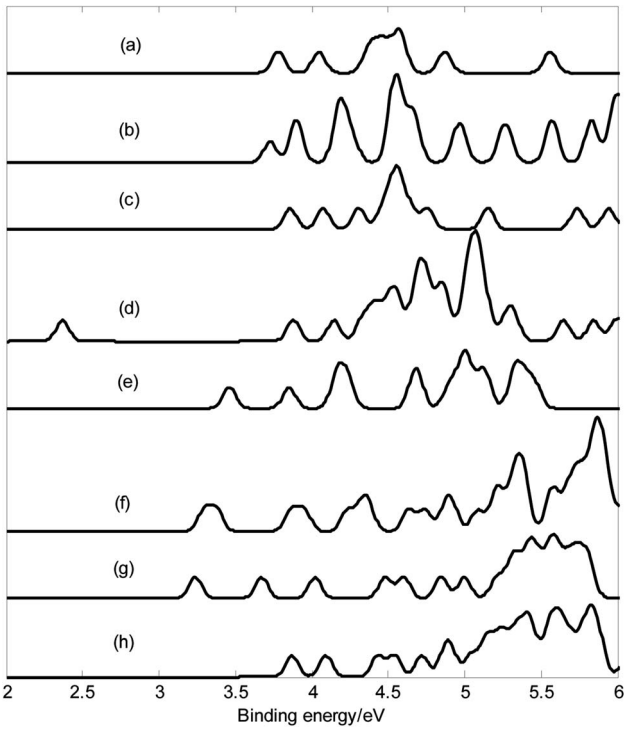

Fig. 4 Calculated photoelectron spectra with PBE0/6-311+G* method. (a) ScB_{24}^-; (b) TiB_{24}^-; (c) VB_{24}^-; (d) CrB_{24}^-; (e) MnB_{24}^-; (f) FeB_{24}^-; (g) CoB_{24}^-; (h) NiB_{24}^-. The simulations were done by fitting the distributions of calculated vertical detachment energies at the PBE0 level with unit-area Gaussian functions of 0.05 eV half-width.

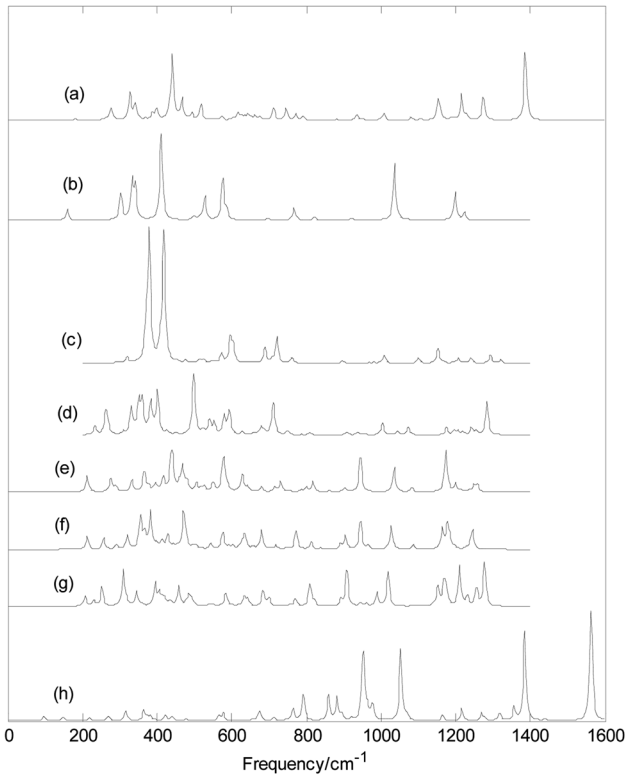

Fig. 5 Calculated infrared spectra with PBE0/6-311+G* method. (a) ScB_{24}^-; (b) TiB_{24}^-; (c) VB_{24}^-; (d) CrB_{24}^-; (e) MnB_{24}^-; (f) FeB_{24}^-; (g) CoB_{24}^-; (h) NiB_{24}^-.

2.37, 3.46, 3.24 and 3.87 eV, respectively. The calculated ground-state VDEs of MB_{24}^- (M = Sc, V, Mn, and Co) originate from the detachment of the electron from the molecular orbital (HOMO). However, for open-shell structure MB_{24}^- (M = Ti, Cr, and Ni), the calculated ground-state VDE of each cluster originates from the detachment of the electron from the singly occupied molecular orbital (α-SOMO). The first peak of FeB_{24}^- comes from the ground-state VDE and second VDE at 3.30 and 3.38 eV, respectively, which originate from detaching the electrons from singly occupied molecular orbital (α-SOMO) and β-HOMO−1, respectively. The second peaks of ScB_{24}^-, VB_{24}^-, MnB_{24}^-, and CoB_{24}^- come from the second calculated VDEs at 4.05, 4.07, 3.85, and 3.67 eV, respectively, which originate from detaching the electrons from HOMO−1. The second peak of TiB_{24}^- comes from the second and third VDEs at 3.90 and 3.89 eV, respectively, which originate from detaching the electrons from singly occupied molecular orbital β-HOMO−1 and β-HOMO−2, respectively. The second peaks of CrB_{24}^- and NiB_{24}^- come from the second VDE at 3.87 and 4.09 eV, respectively, which originate from detaching the electrons from β-HOMO−1. The second peak of FeB_{24}^- comes from the third VDE and fourth VDE at 3.86 and 3.95 eV, respectively, which originate from detaching the electrons from singly occupied molecular orbital β-HOMO−2 and α-HOMO−1, respectively. In addition, the

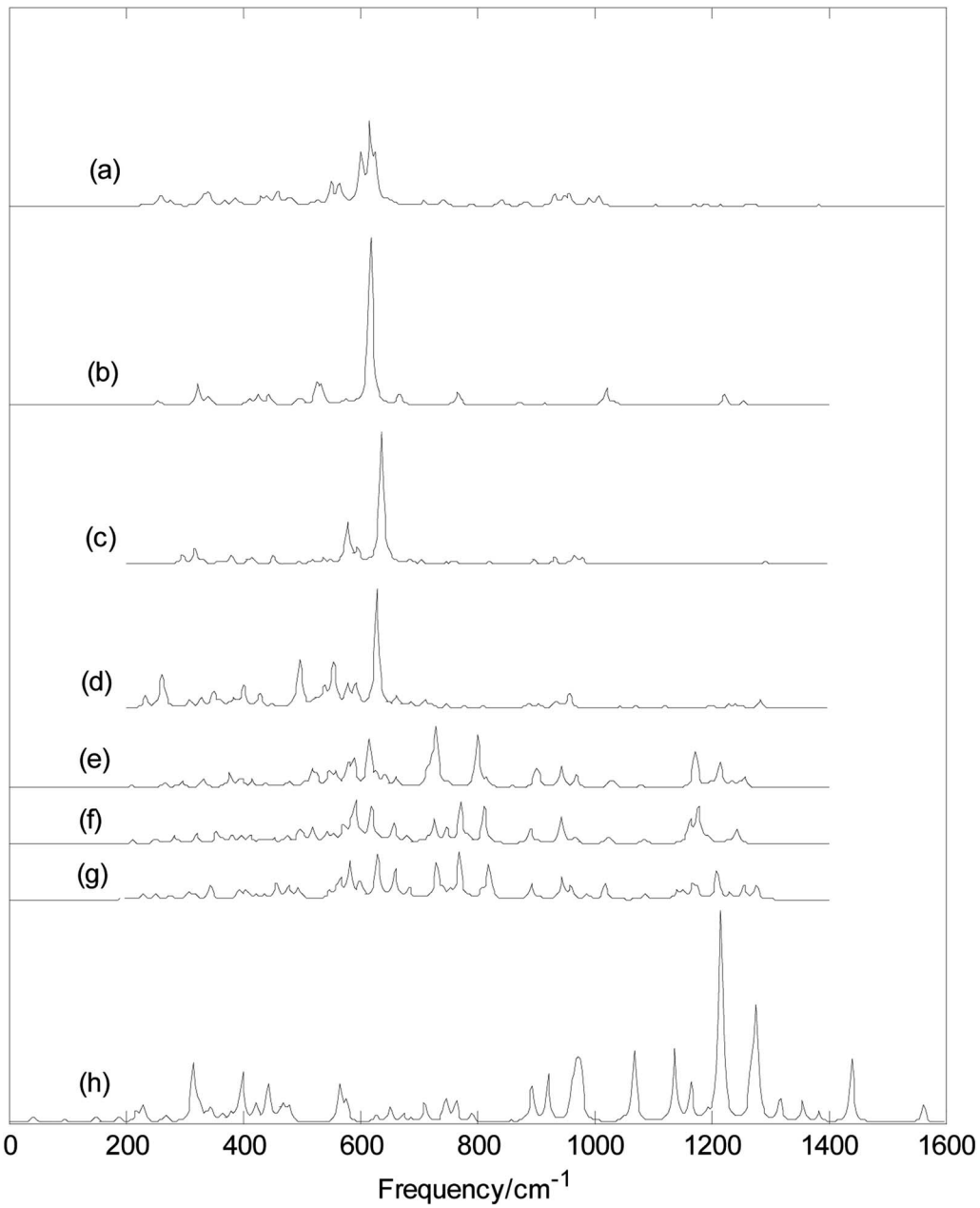

Fig. 6 Calculated Raman spectra with PBE0/6-311+G* method. (a) ScB_{24}^-; (b) TiB_{24}^-; (c) VB_{24}^-; (d) CrB_{24}^-; (e) MnB_{24}^-; (f) FeB_{24}^-; (g) CoB_{24}^-; (h) NiB_{24}^-.

peaks with higher binding energy originate from detaching the electrons from lower molecular orbitals.

Fig. 4 indicates that MB_{24}^- (M = Sc, Ti, V, Cr, Mn, Fe, Co, and Ni) have different spectral features, especially they have different spectral bands at the low binding energy side. These features can be used to distinguish the MB_{24}^- (M = Sc, Ti, V, Cr, Mn, Fe, Co, and Ni) and provide important information for the identification of MB_{24}^- (M = Sc, Ti, V, Cr, Mn, Fe, Co, and Ni). It is worth to note that the structures of clusters cannot directly be identified by common analytical experimental methods, but they can indirectly be determined by using combined theoretical and experimental studies. As the discovery of other anionic boron clusters, if the photoelectron spectra of MB_{24}^- (M = Sc, Ti, V, Cr, Mn, Fe, Co, and Ni) are obtained in experiments, these calculated characteristic bands may be used as theoretical basis for the identification of MB_{24}^- (M = Sc, Ti, V, Cr, Mn, Fe, Co, and Ni).

3.4 Infrared and Raman spectra

Fig. 5 and 6 show plots of the calculated infrared and Raman spectra of MB_{24}^- (M = Sc, Ti, V, Cr, Mn, Fe, Co, and Ni) with PBE0/6-311+G* method. The lowest harmonic frequencies of these clusters are listed in Table 1. From Table 1 and Fig. 5, it can be seen that the cluster structure has a strong influence on the harmonic frequency because these vibration modes are derived from the stretching or bending vibrations of the atoms. Differences in the arrangement of atoms will lead to different modes of vibration. From the calculation results, it can be seen that among the 69 vibration modes of MB_{24}^- (M = Sc, Cr, Mn, Fe, Co, and Ni), all modes are infrared active and Raman active. The calculation results show that among the 69 vibration modes of TiB_{24}^-, 44 modes are infrared-active vibration modes and 25 are inactive modes. Among the 69 vibration modes of TiB_{24}^-, there are 62 Raman-active modes and 7 inactive modes. Among the 69 vibration modes of VB_{24}^-, 55 vibration modes are infrared active and 14 vibration modes are inactive, and only one mode is Raman-inactive mode and other are Raman-active vibration modes. Under the resonance approximation, the infrared intensity is not zero for only the mode where vibration changes the dipole moment and the Raman activity is not zero for only the mode where vibration changes the polarizability. Therefore, all vibration modes of MB_{24}^- (M = Sc, Cr, Mn, Fe, Co, and Ni) can cause changes in polarizability and dipole moment, these vibration characteristics are mainly due to the low symmetry of MB_{24}^- (M = Sc, Cr, Mn, Fe, Co, and Ni). However, for TiB_{24}^-, the 25 infrared inactive modes did not cause changes in dipole moment and the 7 Raman-inactive modes did not cause changes in polarizability. Similarly, for VB_{24}^-, the 14 infrared inactive modes did not cause changes in dipole moment and one Raman-inactive modes did not cause changes in polarizability. These vibration characteristics are mainly due to the high D_{3h} symmetry of TiB_{24}^- and lower C_{2v} symmetry of VB_{24}^-.

It can be seen from Fig. 5 and 6 that MnB_{24}^-, FeB_{24}^-, and CoB_{24} have some similar band characteristics for their similar structure. Although VB_{24}^- and CrB_{24}^- have similar cage structures, they have different infrared spectra. In particular, infrared spectra of VB_{24}^- presents two adjacent strong peaks in the low-frequency region. In addition, from Fig. 6 and the calculation results, the strongest Raman peaks of MB_{24}^- (M = Sc, Ti, V, and Cr) are all located at approximately 620 cm^{-1}, and it maybe due to cage structures of MB_{24}^- (M = Sc, Ti, V, and Cr). The characteristic peaks and band characteristics of these clusters can be used to identify these structures, which can be compared and analyzed in future experiments.

These different results such as the dipole moment, atomic charge, polarizability, and spectral properties are closely related to the structure of clusters. These clusters possess cage structure, tubular structure, and quasi-planar structure, which lead to different electron structures. In addition, the doping of metal atom also has an effect on the electronic structure, as the previous analysis of density of states. Therefore, these clusters show different properties.

4. Conclusions

Research results include the following points. The global minima obtained for the MB_{24}^- (M = Sc, Ti, V, and Cr) clusters correspond to cage structures, and the MB_{24}^- (M = Mn, Fe, and Co) clusters have similar distorted four-ring tube with six boron atoms each. Interestingly, the global minima obtained for the NiB_{24}^- cluster tend to a quasi-planar structure. The electron localization function of MB_{24}^- (M = Sc, Ti, V, Cr, Mn, Fe, Co, and Ni) indicates that the local delocalization of MB_{24}^- (M = Sc, Ti, V, Cr, and Ni) is weaker than that of MB_{24}^- (M = Mn, Fe, and Co), and there is no obvious covalent bond between doped metals and B atoms. Similar to tubular B clusters and deformed B_7 cluster, quasi-planar structure NiB_{24}^-, cage-type MB_{24}^- (M = Sc, Ti, V, and Cr) and tubular MB_{24}^- (M = Mn, Fe, and Co) are expected to become the basic units of boron nanomaterials and be further synthesized into borophene, boron nanotubes or other three-dimensional materials. Considering the electron delocalization characteristics of these clusters, they are expected to be applied to molecular devices or switches. The spin density and spin population analyses reveal that MB_{24}^- (M = Ti, Cr, Fe, and Ni) have different spin characteristics, for example, single electrons of TiB_{24}^- are all alpha electrons and distributed on the Sc and B atoms that can pair with free radicals or small molecules containing beta single electrons to form new covalent bonds. Spin features of these clusters are expected to be applied to catalysis. In addition, these spin features are expected to produce interesting magnetic properties, which will further leads to potential applications in molecular devices. The polarization analysis indicates that MB_{24}^- (M = Mn, Fe, and Co) have larger first hyperpolarizability, indicating that they have strong nonlinear optical response and might be considered as a promising nonlinear optical boron-based nanomaterial. The calculated photoelectron spectra indicate that MB_{24}^- (M = Sc, Ti, V, Cr, Mn, Fe, Co, and Ni) has different characteristic peaks that can be compared with future experimental values and provide a theoretical basis for the identification and confirmation of these single-atom transition metal-doped boron clusters. This research has enriched the structure of single-atom transition metal-doped boron clusters and has certain theoretical

guiding significance for the preparation of new boron nanomaterials, such as borophene and boron nanotubes.

Conflicts of interest

There are no conflicts of interest to declare.

Acknowledgements

This work was supported by the National Natural Science Foundation of China (Grant No. 11804065), the Growth Foundation for Young Scientists of Education Department of Guizhou Province, China (Grant No. QJH KY[2022]310), and the Central Guiding Local Science and Technology Development Foudation of China (Grant No. QK ZYD[2019]4012).

Notes and references

1 H. W. Kroto, J. R. Heath, S. C. O'Brien, R. F. Curl and R. E. Smalley, *Nature*, 1985, **318**, 162–163.
2 S. Iijima, *Nature*, 1991, **354**, 56–58.
3 K. S. Novoselov, A. K. Geim, S. V. Morozov, D. Jiang, Y. Zhang, S. V. Dubonos, I. V. Grigorieva and A. A. Firsov, *Science*, 2004, **306**, 666–669.
4 I. Boustani, *Phys. Rev. B: Condens. Matter Mater. Phys.*, 1997, **55**, 16426–16438.
5 H.-J. Zhai, L.-S. Wang, A. N. Alexandrova and A. I. Boldyrev, *J. Chem. Phys.*, 2002, **117**, 7917–7924.
6 H. J. Zhai, B. Kiran, J. Li and L. S. Wang, *Nat. Mater.*, 2003, **2**, 827–833.
7 B. Kiran, S. Bulusu, H. J. Zhai, S. Yoo, X. C. Zeng and L. S. Wang, *Proc. Natl. Acad. Sci. U. S. A.*, 2005, **102**, 961–964.
8 D. E. Bean and P. W. Fowler, *J. Phys. Chem. C*, 2009, **113**, 15569–15575.
9 Q. Chen, G. F. Wei, W. J. Tian, H. Bai, Z. P. Liu, H. J. Zhai and S. D. Li, *Phys. Chem. Chem. Phys.*, 2014, **16**, 18282–18287.
10 A. P. Sergeeva, I. A. Popov, Z. A. Piazza, W. L. Li, C. Romanescu, L. S. Wang and A. I. Boldyrev, *Acc. Chem. Res.*, 2014, **47**, 1349–1358.
11 T. Jian, X. Chen, S. D. Li, A. I. Boldyrev, J. Li and L. S. Wang, *Chem. Soc. Rev.*, 2019, **48**, 3550–3591.
12 R. Casillas, T. Baruah and R. R. Zope, *Chem. Phys. Lett.*, 2013, **557**, 15–18.
13 H. T. Pham, L. V. Duong, B. Q. Pham and M. T. Nguyen, *Chem. Phys. Lett.*, 2013, **577**, 32–37.
14 J. Lv, Y. Wang, L. Zhu and Y. Ma, *Nanoscale*, 2014, **6**, 11692–11696.
15 H. J. Zhai, Y. F. Zhao, W. L. Li, Q. Chen, H. Bai, H. S. Hu, Z. A. Piazza, W. J. Tian, H. G. Lu, Y. B. Wu, Y. W. Mu, G. F. Wei, Z. P. Liu, J. Li, S. D. Li and L. S. Wang, *Nat. Chem.*, 2014, **6**, 727–731.
16 H. Bai, Q. Chen, H. J. Zhai and S. D. Li, *Angew. Chem., Int. Ed.*, 2015, **54**, 941–945.
17 S.-X. Li, Z.-P. Zhang, Z.-W. Long and S.-J. Qin, *RSC Adv.*, 2017, **7**, 38526–38537.
18 H. Dong, T. Hou, S. T. Lee and Y. Li, *Sci. Rep.*, 2015, **5**, 9952.
19 Y. An, M. Zhang, D. Wu, Z. Fu, T. Wang and C. Xia, *Phys. Chem. Chem. Phys.*, 2016, **18**, 12024–12028.
20 H. Bai, B. Bai, L. Zhang, W. Huang, Y. W. Mu, H. J. Zhai and S. D. Li, *Sci. Rep.*, 2016, **6**, 35518.
21 E. Shakerzadeh, Z. Biglari and E. Tahmasebi, *Chem. Phys. Lett.*, 2016, **654**, 76–80.
22 C. Tang and X. Zhang, *Int. J. Hydrogen Energy*, 2016, **41**, 16992–16999.
23 S. Li, Z. Zhang, Z. Long and D. Chen, *ACS Omega*, 2019, **4**, 5705–5713.
24 S.-X. Li, Z.-P. Zhang, Z.-W. Long and D.-L. Chen, *ACS Omega*, 2020, **5**, 20525–20534.
25 A. J. Mannix, X. F. Zhou, B. Kiraly, J. D. Wood, D. Alducin, B. D. Myers, X. Liu, B. L. Fisher, U. Santiago, J. R. Guest, M. J. Yacaman, A. Ponce, A. R. Oganov, M. C. Hersam and N. P. Guisinger, *Science*, 2015, **350**, 1513–1516.
26 C. Chen, H. Lv, P. Zhang, Z. Zhuo, Y. Wang, C. Ma, W. Li, X. Wang, B. Feng, P. Cheng, X. Wu, K. Wu and L. Chen, *Nat. Chem.*, 2022, **14**, 25–31.
27 Q. Li, V. S. C. Kolluru, M. S. Rahn, E. Schwenker, S. Li, R. G. Hennig, P. Darancet, M. K. Y. Chan and M. C. Hersam, *Science*, 2021, **371**, 1143–1148.
28 I. A. Popov, W. L. Li, Z. A. Piazza, A. I. Boldyrev and L. S. Wang, *J. Phys. Chem. A*, 2014, **118**, 8098–8105.
29 W. Y. Liang, A. Das, X. Dong and Z. H. Cui, *Phys. Chem. Chem. Phys.*, 2018, **20**, 16202–16208.
30 W. Wang, Y.-D. Guo and X.-H. Yan, *RSC Adv.*, 2016, **6**, 40155–40161.
31 R. Saha, S. Kar, S. Pan, G. Martinez-Guajardo, G. Merino and P. K. Chattaraj, *J. Phys. Chem. A*, 2017, **121**, 2971–2979.
32 S.-X. Li, D.-L. Chen, Z.-P. Zhang and Z.-W. Long, *Acta Phys. Sin.*, 2020, **69**, 193101.
33 L. F. Cheung, G. S. Kocheril, J. Czekner and L. S. Wang, *J. Am. Chem. Soc.*, 2020, **142**, 3356–3360.
34 I. A. Popov, T. Jian, G. V. Lopez, A. I. Boldyrev and L. S. Wang, *Nat. Commun.*, 2015, **6**, 8654.
35 T. Jian, W. L. Li, I. A. Popov, G. V. Lopez, X. Chen, A. I. Boldyrev, J. Li and L. S. Wang, *J. Chem. Phys.*, 2016, **144**, 154310.
36 T. T. Chen, W. L. Li, H. Bai, W. J. Chen, X. R. Dong, J. Li and L. S. Wang, *J. Phys. Chem. A*, 2019, **123**, 5317–5324.
37 L. F. Cheung, J. Czekner, G. S. Kocheril and L. S. Wang, *J. Am. Chem. Soc.*, 2019, **141**, 17854–17860.
38 T. T. Chen, W. L. Li, W. J. Chen, X. H. Yu, X. R. Dong, J. Li and L. S. Wang, *Nat. Commun.*, 2020, **11**, 2766.
39 L. F. Cheung, G. S. Kocheril, J. Czekner and L. S. Wang, *J. Phys. Chem. A*, 2020, **124**, 2820–2825.
40 W. J. Chen, M. Kulichenko, H. W. Choi, J. Cavanagh, D. F. Yuan, A. I. Boldyrev and L. S. Wang, *J. Phys. Chem. A*, 2021, **125**, 6751–6760.
41 Z. Y. Jiang, T. T. Chen, W. J. Chen, W. L. Li, J. Li and L. S. Wang, *J. Phys. Chem. A*, 2021, **125**, 2622–2630.
42 S. Chacko, D. G. Kanhere and I. Boustani, *Phys. Rev. B: Condens. Matter Mater. Phys.*, 2003, **68**, 035414.
43 W.-y. Liang, A. Das, X. Dong, M.-h. Wang and Z.-h. Cui, *New J. Chem.*, 2019, **43**, 6507–6512.

44 X. Dong, S. Jalife, A. Vasquez-Espinal, J. Barroso, M. Orozco-Ic, E. Ravell, J. L. Cabellos, W. Y. Liang, Z. H. Cui and G. Merino, *Nanoscale*, 2019, **11**, 2143–2147.
45 J. Lv, Y. Wang, L. Zhang, H. Lin, J. Zhao and Y. Ma, *Nanoscale*, 2015, **7**, 10482–10489.
46 J. Lv, Y. Wang, L. Zhu and Y. Ma, *J. Chem. Phys.*, 2012, **137**, 084104.
47 C. Adamo and V. Barone, *J. Chem. Phys.*, 1999, **110**, 6158–6170.
48 J. Zhang and M. Dolg, *Phys. Chem. Chem. Phys.*, 2015, **17**, 24173–24181.
49 R. Krishnan, J. S. Binkley, R. Seeger and J. A. Pople, *J. Chem. Phys.*, 1980, **72**, 650–654.
50 J. Tao, J. P. Perdew, V. N. Staroverov and G. E. Scuseria, *Phys. Rev. Lett.*, 2003, **91**, 146401.
51 S. Grimme, J. Antony, S. Ehrlich and H. Krieg, *J. Chem. Phys.*, 2010, **132**, 154104.
52 S. Grimme, *Wiley Interdiscip. Rev.: Comput. Mol. Sci.*, 2011, **1**, 211–228.
53 B. Le Chen, W. G. Sun, X. Y. Kuang, C. Lu, X. X. Xia, H. X. Shi and G. Maroulis, *Inorg. Chem.*, 2018, **57**, 343–350.
54 P. Li, X. Du, J. J. Wang, C. Lu and H. Chen, *J. Phys. Chem. C*, 2018, **122**, 20000–20005.
55 S. Jin, B. Chen, X. Kuang, C. Lu, W. Sun, X. Xia and G. L. Gutsev, *J. Phys. Chem. C*, 2019, **123**, 6276–6283.
56 M. Ren, S. Jin, D. Wei, Y. Jin, Y. Tian, C. Lu and G. L. Gutsev, *Phys. Chem. Chem. Phys.*, 2019, **21**, 21746–21752.
57 Y. Tian, D. Wei, Y. Jin, J. Barroso, C. Lu and G. Merino, *Phys. Chem. Chem. Phys.*, 2019, **21**, 6935–6941.
58 M. J. Frisch, G. W. Trucks and H. B. Schlegel, *et al.Gaussian 16*, Gaussian Inc., Wallingford CT, 2016.
59 T. Lu and F. Chen, *J. Comput. Chem.*, 2012, **33**, 580–592.
60 H. Sekino and R. J. Bartlett, *J. Chem. Phys.*, 1993, **98**, 3022–3037.
61 A. Alparone, *Chem. Phys.*, 2013, **410**, 90–98.
62 I. C. Mayer, *Chem. Phys. Lett.*, 1983, **97**, 270–274.
63 A. D. Becke and K. E. Edgecombe, *J. Chem. Phys.*, 1990, **92**, 5397–5403.
64 Q. Chen, W. L. Li, Y. F. Zhao, S. Y. Zhang, H. S. Hu, H. Bai, H. R. Li, W. J. Tian, H. G. Lu, H. J. Zhai, S. D. Li, J. Li and L. S. Wang, *ACS Nano*, 2015, **9**, 754–760.
65 R. Bauernschmitt and R. Ahlrichs, *Chem. Phys. Lett.*, 1996, **256**, 454–464.